

Insights into the Micromechanics of Organic Aerogels Based on Experimental and Modeling Results

Shivangi Aney, Jessica Schettler, Marina Schwan, Barbara Milow, and Ameya Rege*

While the characteristics of the macroscopic mechanical behavior of organic aerogels are well known, the mechanisms responsible for the substructural evolution of their networks under mechanical deformation are not fully understood. Herein, organic aerogels from the aqueous sol–gel polymerization of resorcinol with formaldehyde are first prepared. Specifically, the resorcinol to water (R:W) molar ratio is varied for obtaining diverse highly open-cellular porous structures with mean pore sizes ranging between 30 and 50 nm. The corresponding network structures are then characterized and exhibit different morphological and mechanical properties. Furthermore, a micromechanical constitutive model based on the pore-wall kinematics is proposed. While the arrays of particles forming the pore walls are moderately connected, the pore walls are considered to behave as solid beams under mechanical deformation. Moreover, the damage mechanisms in the pore walls that result in the network collapse are defined. All model parameters are shown to be physically derived, and their sensitivity to the macroscopic network behavior is analyzed. The model predictions are shown to be in good agreement with the experimental stress–strain data of the different aerogels.

of the morphological aspects of RF aerogels on their mechanical performance. Typically for aerogels, like many other open-porous materials, the power law scaling relationship between the Young's modulus E and the bulk density ρ , $E \propto \rho^m$, is often explored in the literature with their mechanical properties. The exponent m was shown to be dictated by the network connectivity.^[11] Considering the open-cell foam model by Gibson and Ashby,^[12] for a perfectly connected open-cellular material, $m = 2$. However, for aerogels, this value ranges between 2 and 4, depending on the type of the aerogel.^[13] Pekala reported exponent values of 2.7 ± 0.2 and 2.4 ± 0.3 for the modulus and compressive strength, respectively, for the case of RF aerogels with envelope densities in the range $0.05\text{--}0.3 \text{ g cm}^{-3}$. Such scaling laws, however, quantify the mechanical properties in the linear elastic regime and give no information about the network damage and the overall mechanical behavior.


1. Introduction

Aerogels from organic sources, e.g., resorcinol formaldehyde (RF), exhibit an open-porous nanostructured morphology having ultralow densities ($0.03\text{--}0.08 \text{ g cm}^{-3}$). The first RF aerogels were synthesized by Pekala^[1] by polycondensation of resorcinol with formaldehyde in an aqueous solution. While investigations on the structural and the thermal properties of RF aerogels have been reported by several authors,^[2–8] reports on their mechanical properties are rare.^[9] Pekala et al.^[10] investigated the dependence

A detailed investigation of the different types of RF aerogels and their mechanical properties was presented by Schwan et al.^[14] There, they analyzed the mechanical behavior of the aerogels by uniaxial compression tests reinforced with digital image correlation measurements, which assisted in further characterizing the evolution of the surface strain gradients, thus giving new insights into the damage (crack) propagation and strain localization over the surface. Hard-to-flexible aerogels were investigated. A subsequent report^[15] on flexible RF aerogels further described the mechanism of their flexibility. An aerogel box model made up of bars (arrays of particles forming the pore wall) was modeled to describe the relation between the flexibility and the relative density.^[16] It is now well known that the macroscopic mechanical behavior of the aerogels is dictated by the microscopic kinematics of their pore walls. By designing a simple framework based on the classical beam theory, it was realized that the lower the aerogel density, the larger the flexibility. Also, the smaller the pore size at a given envelope density, the larger the flexibility. Accordingly, if the density of the string of the pearl network is less than the skeletal density, the flexibility is increased. Such a quadratic-cell model approach was also used to model the micromechanical behavior of biopolymer aerogels.^[17,18]

While approaches such as the diffusion-limited cluster–cluster aggregation (DLCA) have been used to model silica aerogels,^[19,20] such approaches are not suitable for modeling organic aerogels,^[21] as these do not show fractal scaling. In this

S. Aney, J. Schettler, Dr. M. Schwan, Prof. B. Milow, Dr. A. Rege
Department of Aerogels and Aerogel Composites
Institute of Materials Research
German Aerospace Center
Linder Höhe, Cologne 51147, Germany
E-mail: ameya.rege@dlr.de

 The ORCID identification number(s) for the author(s) of this article can be found under <https://doi.org/10.1002/adem.202100095>.

© 2021 The Authors. Advanced Engineering Materials published by Wiley-VCH GmbH. This is an open access article under the terms of the Creative Commons Attribution-NonCommercial License, which permits use, distribution and reproduction in any medium, provided the original work is properly cited and is not used for commercial purposes.

DOI: 10.1002/adem.202100095

study, several RF aerogels based on the recipe of Pekala were synthesized. These are referred through the following text as p-RF aerogels. These were further characterized for their structural and mechanical properties. The mathematical model reported by Schwan et al.^[15] and the constitutive model proposed by Rege et al.^[17] were extended to capture the mechanical behavior of p-RF aerogels. It was recently shown that there is a strong influence of the pore sizes and pore-size distributions on the macroscopic mechanical behavior of aerogels.^[22] In this article, it is further shown that only knowing the pore-size distributions, particle diameters, and skeletal material property of the RF aerogels is sufficient to model and describe their macroscopic mechanical behavior.

2. Methods

2.1. Materials

Resorcinol 98% and anhydrous sodium carbonate were purchased from Aldrich. An aqueous solution of formaldehyde (24% w/w, not stabilized) from VWR, Germany, was used. Acetone (pure, technical grade) was purchased from Th. Geyer, Germany, and deionized water was used for synthesis. For gelation, sealable propylene containers of 120 mL (with screw cap), and for washing, polypropylene containers of 400 mL (press-on lid) were purchased from VWR, Germany. Carbon dioxide 4.5 (purity $\geq 99.995\%$) used for supercritical drying was purchased by Praxair, Germany.

2.2. Synthesis of RF Aerogels

Resorcinol (R) was dissolved at room temperature in deionized water (W) under stirring at 150 rpm using a cross-magnetic stirring bar. The molar ratio R:W was varied from 0.003 to 0.012. The quantities for a 200 mL solution were $m(R_{0.003}) = 3.57$ g and $m(W_{0.003}) = 188.37$ g; $m(R_{0.005}) = 5.84$ g and $m(W_{0.005}) = 180.85$ g; $m(R_{0.009}) = 10.14$ g and $m(W_{0.009}) = 166.66$ g; $m(R_{0.011}) = 12.18$ g and $m(W_{0.011}) = 159.97$ g; and $m(R_{0.012}) = 13.18$ g and $m(W_{0.012}) = 156.78$ g. An aqueous solution of formaldehyde (F) and solid sodium carbonate was then added to the stirred resorcinol solution. The R:C and R:F molar ratios were kept constant at 200 and 0.5, respectively. The pH value of the RF solution was not changed. Stirring at room temperature continued for 30 min, and the homogeneous transparent solution was placed in a sealable polypropylene container in an oven at 60 °C (Mettler GmbH, Germany). After 7 days of gelation and aging, the wet gel was cooled down to room temperature and transferred into an acetone bath to remove residual reagents and exchange water by acetone being soluble in supercritical carbon dioxide. The acetone was refreshed six times within 3 days. Supercritical drying was conducted with CO₂ in an autoclave of 60 L volume (Eurotechnica, Germany) at 60 °C and 110 bars for about 21 h. The degassing rate was adjusted to 0.2 bars per minute.

2.3. Characterization of RF Aerogels

The microstructure of the aerogels was investigated using a scanning electron microscope (SEM) (Zeiss Merlin, Germany). For

specimen preparation, all aerogels were coated with platinum for 90 s with 16 mA. The bulk densities were measured using a GeoPyc instrument and the skeletal densities using an AccuPyc instrument based on displacement measurement techniques (Micromeritics, Germany). For physisorption experiments, the samples were degassed for 12 h at 110 °C and 0.1–0.5 mbar (VacPrep 061, Micromeritics, Germany). The measurements of specific surface area, mesopore volume, and mesopore size distribution were carried out at 77 K by nitrogen adsorption–desorption isotherms (TriStar II, Micromeritics, Germany). The calculations were based on Brunauer–Emmett–Teller (BET) and Barrett–Joyner–Halenda (BJH) methods. The mechanical testing was conducted using an INSTRON 5566A (INSTRON, United Kingdom) and load cells of 500 N. The compression was conducted at a rate of 1 mm min⁻¹. For measuring the nominal stress from the applied force, the specimen cross-sectional area was measured using a digital microscope Keyence VHX-1000D (Keyence Corporation, Germany).

2.4. Constitutive Modeling

The mechanical properties of cellular solids can be formulated based on the mechanics of their pore walls.^[12] p-RF aerogels exhibit a cellular morphology, and their microscopic characteristics will be discussed in detail in Section 3. The aerogel network is made up of arrays of particles connected together in a 3D open-porous network. These arrays of particles then form the pore walls. Dargazany et al.^[23] investigated the validity of representing interparticle bonds by means of linear springs. They found that under relatively small deformations and for moderately connected bonds, this assumption remains valid. Furthermore, Schwan et al.^[15] modeled the flexibility in carbon aerogels by assuming the array of particles to behave as a solid beam. Building upon these studies, and considering the microcell model by Rege et al.,^[17] the open-cellular network of p-RF aerogels was assumed to be made up of a network of quadratic microcells distributed homogeneously through the 3D network. The pore wall (or walls of these microcells) was considered to have the diameter of the particle (d_p). An illustration of the model

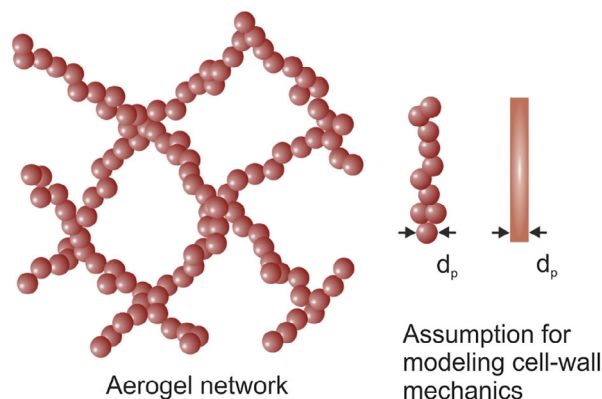


Figure 1. Illustration of the cellular aerogel network and the assumption of the equivalency between the array of particles forming the pore wall and a beam with a circular cross section having the same diameter as that of the particles.

Table 1. Properties of RF aerogels as a function of R:W molar ratio.

R:W molar ratio	Envelope density [g cm ⁻³]	Skeletal density [g cm ⁻³]	Porosity [%]	Pore volume [cm ³ g ⁻¹]	BET surface area [m ² g ⁻¹]	Mesopore volume [cm ³ g ⁻¹]	Average pore diameter [nm]	Average particle size [nm]
0.003	0.10	1.72	94.2	9.42	496	2.48	76 ^{a)} ; 49 ^{b)}	7.0
0.005	0.11	1.62	92.9	8.10	509	3.50	64 ^{a)} ; 38 ^{b)}	7.3
0.009	0.15	1.49	89.9	5.94	526	2.77	45 ^{a)} ; 35 ^{b)}	7.6
0.011	0.17	1.45	88.2	5.16	449	3.88	46 ^{a)} ; 33 ^{b)}	9.2
0.012	0.18	1.49	87.9	4.91	514	2.43	38 ^{a)} ; 33 ^{b)}	7.8

^{a)}Calculated with Equation (9); ^{b)}Calculated from the peak maximum of the pore size distribution.

assumption is shown in **Figure 1**. The values for the different cases of the p-RF aerogels are shown in **Table 1**. The pore wall was then modeled as an Euler–Bernoulli beam. The variation in the sizes of the microcells was approximated by means of BJH pore-size data. Such an approach was shown to be suitable for modeling the fibrillar network of the biopolymer aerogels.^[18] Thus, the proposed model was an extension of the aforementioned models, in a way suitable for p-RF aerogels. These pore walls were represented as isotropic and homogeneous beams of constant circular cross section.

2.4.1. Model Description

The aerogel network was assumed to be formed of isotropically and continuously distributed microcells in all spatial directions. Under compression, the pore walls underwent axial compression and bending. The force acting on the pore wall was split into an axial component and a bending one. The derivation of the strain energy of a quadratic cell under deformation is already shown in the study by Rege and Itskov.^[24] In terms of the microscopic stretches (λ), the strain energy can be expressed as

$$\psi(\lambda, l) = \frac{2E(1-\lambda)^2 \sin^2 \varphi}{l} [3I \cos^2 \varphi + Al^2 \sin^2 \varphi] \quad (1)$$

where l represents the length of the pore wall and E , I , and A denote the Young's modulus, area moment of inertia, and cross-sectional area of the pore wall.

2.4.2. Distribution of Pore Sizes

The varying pore sizes in the p-RF aerogel network were determined by the BJH method^[19] and are described in greater detail in Section 3. Using the pore-area distribution, the probability density function of the pore sizes ($p(l)$) was calculated. This is usually non-Gaussian, and previous studies have used a generalized beta distribution function to mathematically describe it. However, in this work, a normal distribution function approximated the pore-size density much better than the non-Gaussian ones. Accordingly, $p(l)$ along the range of the pore-wall lengths (l) is expressed as

$$p(l) = \frac{1}{\vartheta \sqrt{2\pi}} e^{-\frac{(x-l_{\text{mean}})^2}{2\vartheta^2}} \quad (2)$$

where l_{mean} and ϑ denote the mean and standard deviation of the function. These parameters were obtained by approximating $p(l)$ to the BJH data.

2.4.3. Damage Criteria

Substructural evolution in the aerogel network leads to damage due to the breaking of the interparticle bonds. The failure in an array of particles is assumed to occur when the bending moment between the particles reaches a critical value. Unlike in our previous model, this was translated to the bending stress of the beam (pore wall), which is $\frac{M}{Z}$, where M is the bending moment and Z is the section modulus of the pore wall. The bending stress is accordingly expressed in terms of the microstretches as

$$\sigma_{\text{ben}(\lambda, l)} = \frac{3Ed_p(1-\lambda) \sin \varphi \cos \varphi}{2l} \quad (3)$$

Once this bending stress reached a maximum allowable value σ_{max} , the cell walls lost their mechanical integrity and resulted in pore collapse. The collapsed cell walls did not contribute to the total network energy. This collapse of the pores had an influence on the evaluation of the network strain energy. The 1D network energy in any spatial direction d is given by

$$\Psi^d = \int_{l_m(\lambda^d)}^{l_{\text{max}}} N_p p(l) \psi(l, \lambda^d) dl \quad (4)$$

where N_p is the total number of microcells within the network and λ^d is the microstretch in direction d . As only the active cells contribute to the network, the limits of the integral change with increasing deformation. In the reference configuration, $l_m(\lambda^d) = l_{\text{min}}$.

2.4.4. Directional Averaging

For generalizing the 1D network response to 3D, the concept of numerical integration over a unit microsphere was used.^[15] This approach was proven to be useful in modeling cellular solids.^[17,25] Accordingly, the 3D network strain energy can be expressed as

$$\Psi \approx \sum_{i=1}^k \omega_i \Psi^d = \sum_{i=1}^k \omega_i \int_{l_m(\lambda^{d_i})}^{l_{\text{max}}} N_p p(l) \psi(l, \lambda^{d_i}) dl \quad (5)$$

where ω_i represent the weight factors corresponding to the collocation directions d_i . In our model, the scheme of numerical integration with $k = 45$ integration points over the half sphere was used.

The macroscopic first Piola–Kirchhoff (nominal) stress tensor T can be then expressed as

$$T = \frac{\partial \Psi}{\partial F} = \frac{\partial \Psi}{\partial \lambda^{d_i}} \frac{\partial \lambda^{d_i}}{\partial F} \quad (6)$$

where F denotes the deformation gradient. Affine deformation was assumed, such that the microscopic stretches followed the macroscopic ones.

3. Results and Discussion

3.1. Experimental Analysis

3.1.1. Properties and Microstructure of RF Aerogels

The prepared aerogels showed a dark red color with translucence and exhibited a hard and brittle surface. As expected, the increase

of solid content in the synthesis procedure resulted in an increase in the envelope density, as shown in **Figure 2a**.

The porosity Φ was calculated from envelope and skeletal densities (ρ_e and ρ_s), as

$$\Phi = 1 - \frac{\rho_e}{\rho_s} \quad (7)$$

Figure 2a also shows that the porosity decreased with increasing solid content (R:W molar ratio).

The microstructure of the p-RF aerogels was qualitatively investigated using a SEM. Figure 2c,d shows the micrographs of the aerogels, prepared with the lowest and the highest solid content (R:W molar ratio). The micrographs of the other aerogels with intermediate solids contents are shown in Figure S1, Supporting Information. It can be seen that all aerogels have a very homogeneous nanostructure with a high degree of cross-linking. The network consists of small particles, linked together like a string of pearls. A higher concentration of resorcinol and formaldehyde leads to denser structures and higher cross-linking. The particle size increases, whereas the pore size decreases. To validate these observations, the average pore size d_{pore} is calculated using Equation (9).

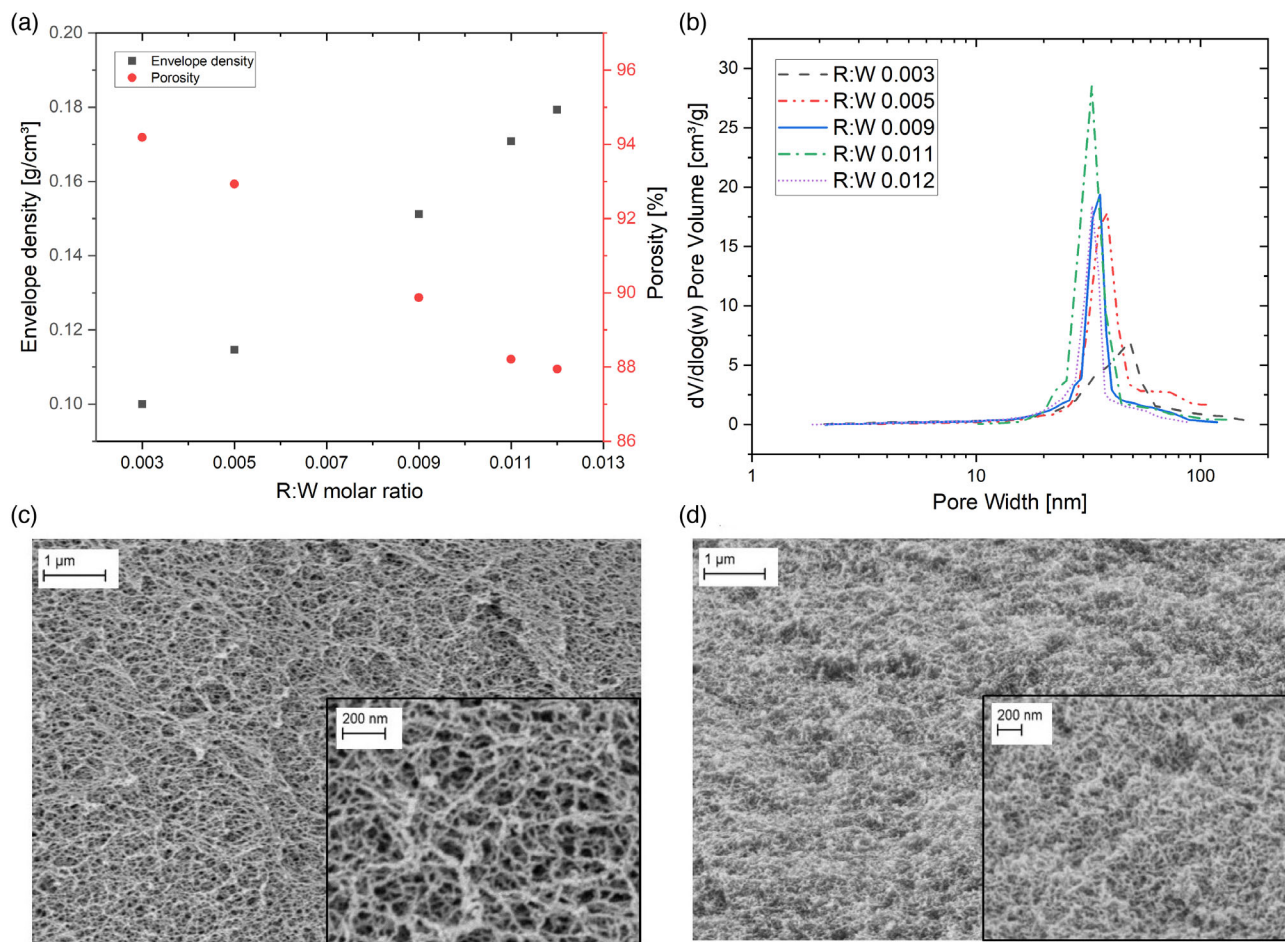


Figure 2. a) Increase in envelope density and decrease in porosity with a higher resorcinol amount. b) Pore size distributions of RF aerogels with increasing solid content (R:W molar ratio) and microstructure of aerogels prepared at R:W molar ratios of c) 0.003 and d) 0.012.

$$V_{\text{pore}} = \frac{1}{\rho_e} - \frac{1}{\rho_s} \quad (8)$$

$$d_{\text{pore}} = \frac{4 \cdot V_{\text{pore}}}{S_{\text{BET}}} \quad (9)$$

The average particle size d_p can be calculated using the BET surface area (S_{BET}) and ρ_s , as

$$d_p = \frac{6}{S_{\text{BET}} \cdot \rho_s} \quad (10)$$

The results are shown in Table 1.

The calculations confirmed the observations from the SEM images. Table 1 shows that the particle size exhibited an increasing trend with increasing solid content, whereas the pore diameter strongly decreased. While a clear trend in the BET surface area could not be identified, the increase in particle size was attributed to the corresponding decrease in the skeletal density. Looking at the pore size distributions shown in Figure 2b, it is also evident that the mean pore size decreased with increasing solid content and the pore size distribution became narrower.

3.1.2. Mechanical Properties

The mechanical properties were investigated under uniaxial compression. The stress–strain curves showed the typical nature found in cellular materials (Figure 3).^[26] At first, a linear elastic regime was observed, where the increment in stress was directly proportional to the compressive strain. This region is also known as Hooke's region and there, the deformation is reversible. The slope of the curve in this region quantifies the Young's modulus, which was found to increase with increasing solid content (increasing R:W ratio). For samples with R:W 0.003 and 0.005, the linear region was less pronounced, whereas for other samples, it was distinct. Figure 4 shows the evaluated Young's modulus versus the envelope density. A higher solid content

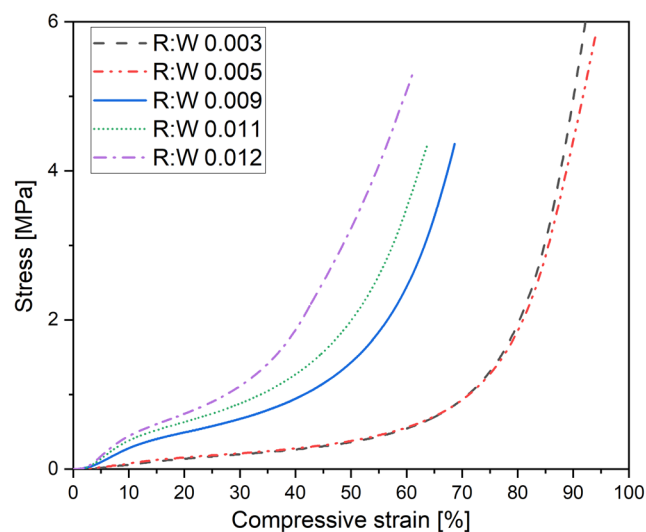


Figure 3. Stress–compressive strain curves of RF aerogels with different R:W molar ratios.

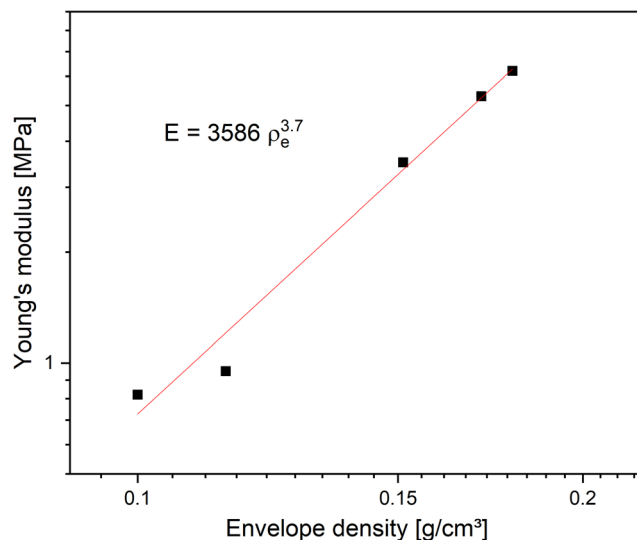


Figure 4. Log–log plot of calculated Young's modulus versus envelope density.

leads to a denser and more cross-linked structure, resulting in an increase in the stiffness. The stress–strain curves, presented in Figure S2, Supporting Information, show a high reproducibility of the results, up to a compressive strain of less than 30%.

Beyond the linear elastic regime, a plateau was observed. There, nonreversible deformation occurred. The pore walls were deformed, due to bending and subsequent failure, leading to pore collapse. The plateau regime for samples with low R:W molar ratios was longer and continued up to around 50% of compression, whereas the plateau for other samples was short and ended at around 20%. These differences were attributed to the different mean pore sizes of the samples. As shown in Table 1, the average pore size changes with increased R:W ratio. The larger the pores, the longer they deformed to achieve a compact, less porous structure. The final regime is called the

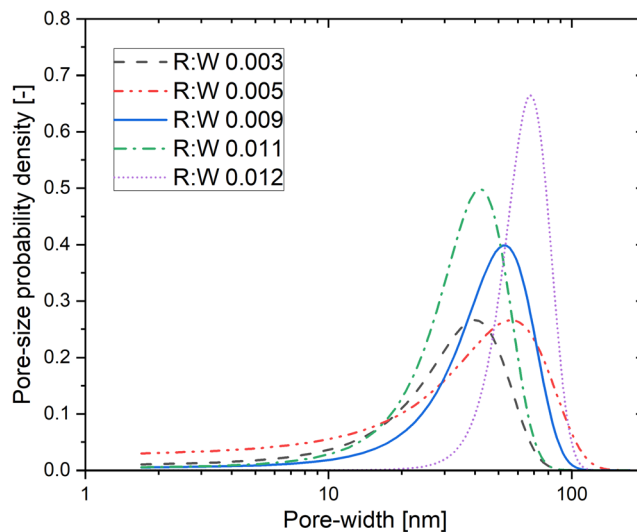


Figure 5. Approximated pore-size probability density for the different p-RF aerogels.

densification regime. In this region, the stress increased rapidly for all samples. There, the porous structure of aerogels was completely destroyed.

The exponent m from the scaling relation between the Young's modulus (E) and the envelope density (ρ_e) was found to be 3.7, which is typical for aerogels.^[13] Pekala et al.^[10] reported an exponent of 2.7 ± 0.2 for RF aerogels, whereas Groß and Fricke^[13] reported one with 3.13 ± 0.07 . The differences may have been caused from different synthesis parameters, e.g., aging temperature and curing step. Especially during aging and curing, the connectivity between the particles changes, which affects the mechanical response of RF aerogels. The prefactor, in our study, was $10^{3.55}$.

3.2. Model Evaluation

3.2.1. Model Parameter Analysis

The proposed model consisted of four material constants (l_{\min} and l_{\max} , minimum and maximum length of the cell walls;

d_p , particle diameter or diameter of the cell wall approximated as a beam; and E , the Young's modulus of the cell wall) and two fitting parameters (N_p , the initial number of microcells in the network and σ_{\max} , the maximum allowable bending stress in a cell wall).

Among these, the parameters l_{\min} and l_{\max} were determined directly from the limits of the pore-size distributions obtained through the BJH data. The BJH data (Figure 2b) were used to obtain the PDF of the pore sizes, which were then fit by means of a normal distribution function for the different types of p-RF aerogels (with varying molar ratios). The corresponding distributions are shown in the Figure 5. The sensitivity of the model response to variations in different material parameters, viz., the particle diameter d_p , initial number of microcells N_p , mean pore size l_{mean} , and maximum allowable bending stress σ_{\max} , was studied (see Figure 6). Such a parameter sensitivity analysis was executed by varying only the concerned parameter, while maintaining all other material parameters constant. It was observed that σ_{\max} had a strong influence on the collapse of the microcells

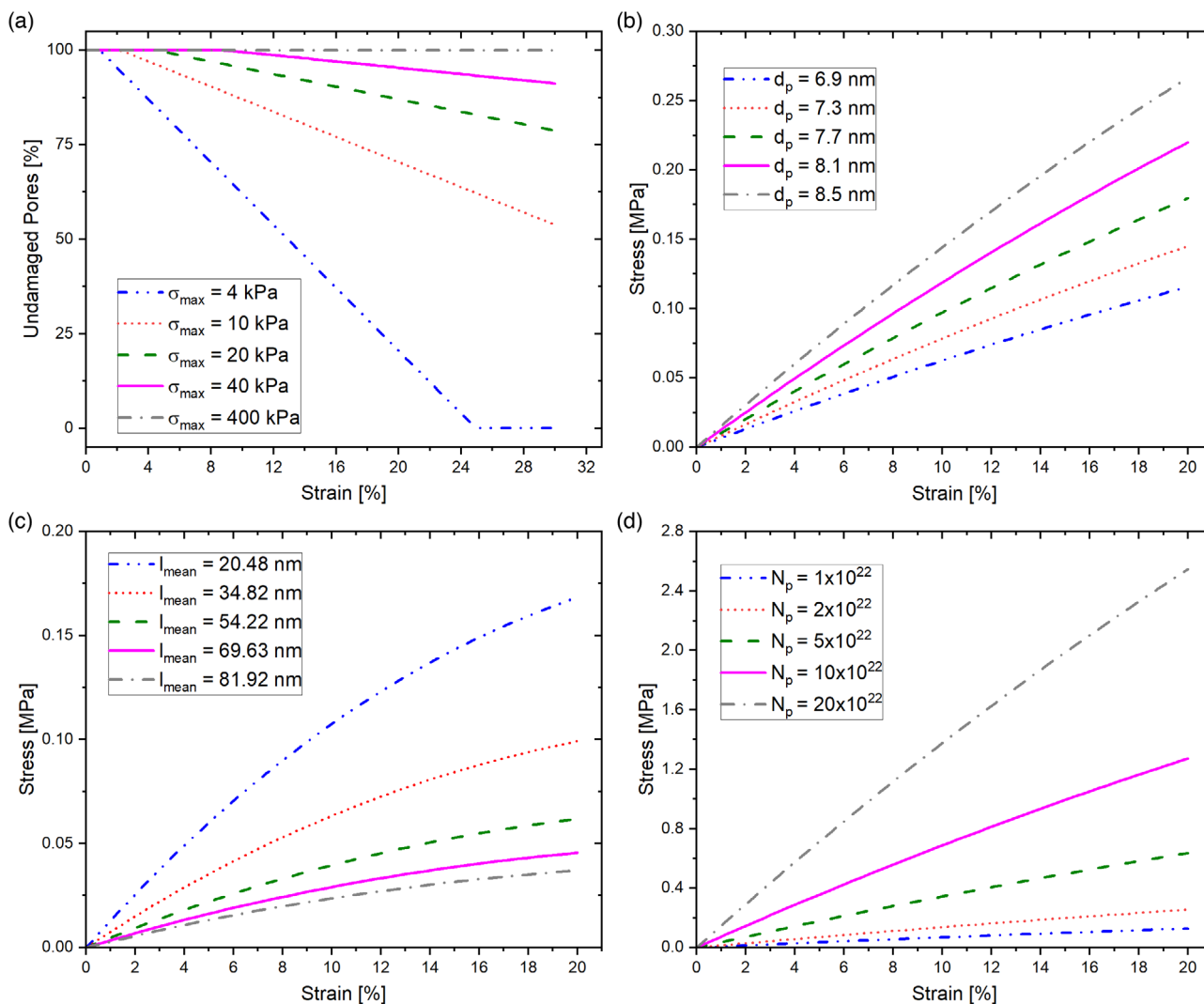


Figure 6. Parameter sensitivity analysis: Influence of variations in a) σ_{\max} , b) d_p , c) l_{mean} , and d) N_p on the macroscopic aerogel network behavior.

(see Figure 6a). As the allowable bending moment was reduced, the microcells started to collapse sooner at lower strains. The material response, thus, became more brittle. The parameters d_p and N_p had a multiplicative effect on the stress–strain response of the network, as shown in Figure 6b,d. Thus, increasing them resulted in a stiffening of the network response. However, no changes in the nature of the stress–strain response were observed. Figure 6c shows that the mean pore size had a significant effect on the macroscopic compressive behavior. The smaller the mean pore size of the aerogel network, the stiffer the network response.

Although σ_{\max} could not be correlated with the synthesis parameters, its significant influence on the collapse of the microcells is shown in Figure 6a. Thus, the parameter analysis could be useful to support in tailoring the mechanical properties of p-RF aerogels.

3.2.2. Validation with Experimental Results

The model predictions, as obtained from Equation (6), were validated with the experimental data and are shown in Figure 7. While the model is not yet designed to capture the densification in the aerogel network, beyond the pore collapse, the model could only predict the stress–strain behavior up to 10–12% strain. Good agreement between the two can be observed. The proposed constitutive model could thus describe the linear elastic regime and a portion of the plateau regime before densification took effect. Subsequently, the model predictions deviated from the experimental results with the onset of densification. This was seen more distinctly for the molar ratios 0.009, 0.011, and 0.012, whereas they showed early densification (see Figure 3).

The model parameters are shown in Table 2. As discussed earlier, l_{\min} , l_{\max} , and d_p were directly obtained from the experimental characterization data. The skeletal Young's modulus E was calculated using the scaling relationship by Gibson and Ashby, as the parameters ρ_s , ρ_e , E_{bulk} , and m were already known. It was estimated to be 4.4 ± 0.4 MPa for molar ratios 0.005, 0.009, 0.011, and 0.012, with the exception of R:W molar ratio

Table 2. Model parameters for the different p-RF aerogels.

R:W molar ratio	l_{\min} [nm]	l_{\max} [nm]	d_p [nm]	E [MPa]	$N_p^{a)}$ [-]
0.003	1.7	173.6	7.0	8.5 ± 0.0	6.0×10^{25}
0.005	3.6	102.4	7.3	4.4 ± 0.4	7.6×10^{25}
0.009	2.3	102.0	7.6		2.7×10^{26}
0.011	5.8	108.9	9.2		3.6×10^{26}
0.012	2.0	75.0	7.8		7.0×10^{26}

^{a)}Parameter obtained from model fitting; all other parameters were obtained directly from experimental data.

0.003, where it was reported to be 8.5 MPa. Although N_p was a fitting parameter, it clearly increased with increasing R:W molar ratio. This agreed well with the SEM image analysis, viz., the higher the R:W molar ratio, the denser the aerogel network. The bending stress criterion captured the damage in the pore walls and was shown to predict the pore collapse in the aerogel network.

The micromechanical nature of the model described the sub-structural evolution in p-RF aerogels under deformation. It is interesting to note that the model predicted the stress–strain curves of the different RF aerogels despite the fact that they showed a scaling exponent of $m = 3.7$. Such modeling approaches were so far validated with biopolymer aerogels, e.g., cellulose based, which show an exponent of nearly 2,^[27] thus within the realms of the open-cell foam model by Gibson and Ashby.^[12] As the proposed modeling approach was based on the pore-wall mechanics and accounted for the pore-size distribution, as obtained from the experimental data, the model was capable of accurately describing the constitutive behavior of the aerogels that did not adhere to the scaling exponent in accordance with the open-cell foam model. The validation results indicate a possible application of this model to predict the constitutive behavior for different p-RF aerogels as long as the network pore-size distribution and particle diameter for different molar ratios are known a priori. A few molar ratios such as 0.03 may be exceptions, where additional input parameters may be needed to be investigated before the macroscopic behavior can be predicted.

4. Conclusion

In this article, resorcinol formaldehyde aerogels with different R:W molar ratios were synthesized and characterized. Small changes in the molar ratio showed significant changes to their morphological as well as mechanical properties. While the envelope density and the average particle diameter increased with increasing R:W ratio, quantities such as the skeletal density, porosity, pore volume, and the average pore diameter correspondingly decreased. Also, the higher the R:W ratio, the stiffer the mechanical performance. Interestingly, the overall stress–strain curve of the aerogels with R:W ratios 0.003 and 0.005 coalesced through most of the course of their deformation, whereas the ones for the other R:W ratio remained distinctly apart. New insights into the pore collapse and the effects of different

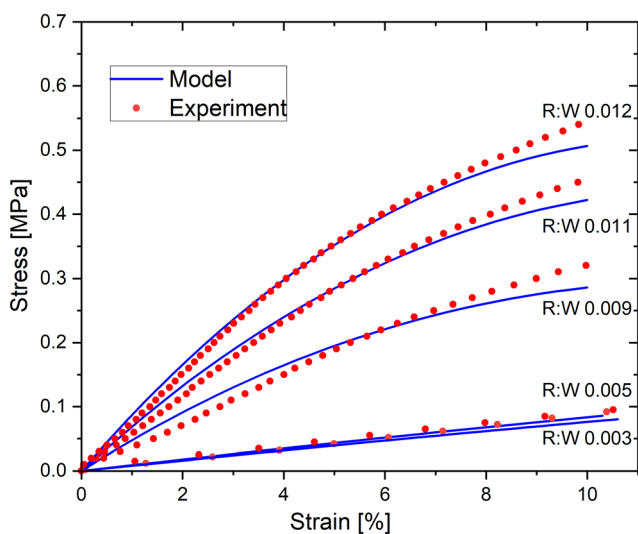


Figure 7. Validation of model predictions with experimental results.

morphological aspects on the macroscopic mechanical behavior of the aerogels were presented by means of a micromechanical model. The constitutive model was based on the mechanics of the pore walls, which were modeled as solid beams. All model parameters were physically motivated, and their effect on the macroscopic network behavior was studied. While a few parameters, namely, the Young's modulus of the pore walls, the particle diameter, and the initial number of cells, only had a multiplicative effect on the overall macroscopic behavior, the pore-size distribution and the critical bending stress in the pore walls influenced the nature of the network behavior. The model predictions showed good agreement with the experimental data of the p-RF aerogels under compression. The model was successful in describing the network behavior in the linear elastic regime and a part of the plateau regime. The initiation of the pore collapse, as predicted by the model, agreed with the softening in the corresponding experimental stress–strain curve. The applicability of the proposed model to describe the mechanical properties of other organic aerogels, apart from the biopolymeric ones and the presented p-RF ones, is yet unknown.

Received: January 25, 2021

Revised: March 22, 2021

Published online:

Supporting Information

Supporting Information is available from the Wiley Online Library or from the author.

Acknowledgements

The authors acknowledge Benjamin Ignatzi and Rebekka Probst for their support in experiments, analysis, and for SEM images. S.A. acknowledges the DLR-DAAD Research Fellowship Program.

Open access funding enabled and organized by Projekt DEAL.

Conflict of Interest

The authors declare no conflict of interest.

Data Availability Statement

Research data are not shared.

Keywords

mechanical properties, micromechanical modeling, organic aerogels, pore-wall mechanics, resorcinol formaldehyde

- [1] R. W. Pekala, *J. Mater. Sci.* **1989**, *24*, 3221.
- [2] F. Despetis, K. Barral, L. Kocon, J. Phalippou, *J. Sol-Gel Sci. Technol.* **2000**, *19*, 829.
- [3] T. Horikawa, J. I. Hayashi, K. Muroyama, *Carbon* **2004**, *42*, 169.
- [4] C. J. Gommès, A. P. Roberts, *Phys. Rev. E* **2008**, *77*, 041409.
- [5] O. Czakkel, B. Nagy, E. Geissler, K. László, *J. Supercrit. Fluids* **2013**, *75*, 112.
- [6] M. Alshrah, M.-P. Tran, P. Gong, H. E. Naguib, C. B. Park, *J. Colloid Interface Sci.* **2017**, *485*, 65.
- [7] R. Tannert, M. Schwan, A. Rege, M. Eggeler, J. C. da Silva, M. Bartsch, B. Milow, M. Itskov, L. Ratke, *J. Sol-Gel Sci. Technol.* **2017**, *84*, 391.
- [8] E. Martin, M. Prostredny, A. Fletcher, P. Mulheran, *Gels* **2020**, *6*, 23.
- [9] S. L. Flores-López, B. Karakashov, L. A. Ramírez-Montoya, J. A. Menéndez, V. Fierro, A. Arenillas, M. A. Montes-Morán, A. Celzard, *J. Mater. Sci.* **2021**.
- [10] R. W. Pekala, C. T. Alviso, J. D. LeMay, *J. Non-Cryst. Solids* **1990**, *125*, 67.
- [11] H.-S. Ma, A. P. Roberts, J.-H. Prévost, R. Jullien, G. W. Scherer, *J. Non-Cryst. Solids* **2000**, *277*, 127.
- [12] L. J. Gibson, M. F. Ashby, *Cellular Solids: Structure and Properties*, Cambridge University Press, Cambridge, UK **1999**.
- [13] J. Groß, J. Fricke, *Nano Struct. Mater.* **1995**, *6*, 905.
- [14] M. Schwan, M. Naikade, D. Raabe, L. Ratke, *J. Mater. Sci.* **2015**, *50*, 5482.
- [15] M. Schwan, R. Tannert, L. Ratke, *J. Supercrit. Fluids* **2016**, *107*, 201.
- [16] J. C. H. Wong, H. Kaymak, S. Brunner, M. M. Koebel, *Microporous Mesoporous Mater.* **2014**, *183*, 23.
- [17] A. Rege, M. Schestakow, I. Karadagli, L. Ratke, M. Itskov, *Soft Matter* **2016**, *12*, 7079.
- [18] A. Rege, I. Preibisch, M. Schestakow, K. Ganesan, P. Gurikov, B. Milow, I. Smirnova, M. Itskov, *Materials* **2018**, *11*, 1670.
- [19] A. Hasmy, E. Anglaret, M. Foret, J. Pelous, R. Jullien, *Phys. Rev. B* **1994**, *50*, 6006.
- [20] R. Abdusalamov, C. Scherdel, M. Itskov, B. Milow, G. Reichenauer, A. Rege, *J. Phys. Chem. B* **2021**, *125*, 1944.
- [21] A. P. Roberts, *Phys. Rev. E* **1997**, *55*, R1286.
- [22] A. Rege, S. Aney, B. Milow, *Phys. Rev. E* **2021**.
- [23] R. Dargazany, H. Chen, J. Lin, A. I. Azad, A. Alexander-Katz, *Polymer* **2017**, *109*, 266.
- [24] A. Rege, M. Itskov, *Acta Mech.* **2018**, *229*, 585.
- [25] T. Bleistein, A. Jung, S. Diebels, *Continuum Mech. Thermodyn.* **2019**, *32*, 255.
- [26] M. F. Ashby, R. F. M. Medalist, *Metall. Trans. A* **1983**, *14*, 1755.
- [27] S. Zhao, W. J. Malfait, N. Guerrero-Alburquerque, M. M. Koebel, G. Nyström, *Angew. Chem., Int. Ed.* **2018**, *57*, 7850.